Journal of Visualization, Vol. 9, No. 2 (2006)145-160

Heat Transfer and Fluid Flow of Benard-Cell Convection in Rectangular Container with Free Surface Sensed by Infrared Thermography

Inagaki, T.*[1], Hatori, M.*[1], Suzuki, T.*[1] and Shiina, Y.*[2]

*1 Dept. Mech. Eng., Ibaraki University, 12-1 Nakanarusawa 4 Chome, Hitachi, Ibaraki, 316-8511, Japan. Tel: +81-294-38-5044/Fax: +81-294-38-5044, E-mail: hotaru@mx.ibaraki.ac.jp
*2 Japan Atomic Energy Research Institute, 3607 Arahori Narita Oarai, Higashiibaraki, Ibaraki, 311-1934, Japan. Tel: +81-29-264-8705/Fax: +81-29-264-8710, E-mail: shiina@spa.oarai.jaeri.go.jp

Received 29 March 2005
Revised 25 October 2005

Abstract : The natural convection flow phenomena that occur inside an enclosed space are very interesting examples of complex fluid systems that may yield to analytical, empirical and numerical solutions, and many reports have looked into this basic problem. In the present study, heat transfer and fluid flow for natural convection in a horizontal rectangular container with a free surface are investigated using infrared thermography. The temperature field was measured and visualized at a gas-liquid (air - silicon oil) interface using infrared thermography. The heat transfer phenomena were also investigated by statistically analyzing the temperature data. The applicability of the infrared thermography to quantitative heat transfer measurement at the gas-liquid interface was evaluated. It is revealed that infrared thermography is effective not only in visualization of a gas-liquid interface but also in heat transfer measurement. A new heat transfer correlation is proposed for the gas-liquid interface of this flow system. The coefficient of heat transfer can be summarized by a specific heat transfer correlation formula regardless of several conditions, including container aspect ratio, fluid viscosity and fluid layer depth.

Keywords : Infrared Thermography, Thermal Visualization, Gas-liquid Interface, Heat Transfer, Natural Convection, Turbulence.

1. Introduction

Infrared thermography is convenient for a variety of engineering applications because it enables characterization of every pixel nondestructively and simultaneously over a two-dimensional temperature field. Infrared thermography (e.g., Kamoi, 2002) detects the thermal energy emitted from an object as electromagnetic waves and evaluates the surface temperature field nondestructively. The technique can also characterize two-dimensional temperature fields with any complicated shapes using real-time pixels. Infrared thermography has mainly been utilized for measuring heat transfer from solid surfaces in the field of heat transfer science (Inagaki, 1999), however, there it is not well known whether the technique can be effectively applied to measurement of gas-liquid interfaces. Heat transfer measurement at the gas-liquid interface is expected to be difficult for sensors other than optical sensors that are attached at the interface. This is because it is difficult to install the non-optical sensors at a gas-liquid interface correctly. Several experimental

and analytical results (e.g., Cerisier, 1996) have been presented on the phenomena that occur by Benard-cell convection. However, little work has addressed the interface phenomenon for Benard-cell convection or turbulent convection while considering flow with a free surface. A few investigations (Asaeda, 1982; Asaeda, 1983) have investigated the flow phenomena as an example of the specific interface phenomenon for a free surface.

The present study therefore investigates Benard-cell convection and turbulent convection in a limited rectangular container with a free surface as a representative example of heat transfer phenomena at a gas-liquid interface. The temperature fields generated by Benard-cell convection and turbulent convection were visualized and measured at the gas-liquid (air - silicon oil) interface using infrared thermography. The applicability and effectiveness of infrared thermography were confirmed by experimental investigation and numerical computation.

2. Nomenclature

A_0 : Area of rectangular container (Hydraulic area) (= W_1 W_2) [m^2]

$C_{\varepsilon 1}$, $C_{\varepsilon 2}$, C_μ : Model constants [-]

f_1, f_2, f_μ : Model functions [-]

g : Gravitational acceleration [m/s]

h : heat transfer coefficient ($= \dfrac{q - q_{rad}}{\overline{T}_s - T_g}$)

I : Input current [A]

l : Distance between gas-liquid interface and infrared sensor [m]

n : Coordinates [m]

Nu_g : Nusselt number in gas phase ($= \dfrac{hW_e}{\lambda}$) [-]

Nu_l : Nusselt number in liquid phase ($= \dfrac{q\delta}{\lambda(T_w - T_c)}$) [-]

P : Pressure [Pa]

Pr_g : Prandtl number of gas [-]

Pr_l : Prandtl number of liquid [-]

Pr_t : Turbulent Prandtl number [-]

P_κ : Turbulent production [m^2/s^3]

q : Net heat flux [W/m^2]

q_{Joule} : Amount of Joule heating ($= \dfrac{VI}{A_0}$) [W/m^2]

q_{loss} : Loss to backside of container [W/m^2]

Ra_l : Rayleigh number in fluid layer ($= \dfrac{g\beta_l(T_W - T_{g'})\delta^3}{\nu_l^2} Pr_l$) [-]

Ra_{lc} : Critical Rayleigh number in fluid layer [-]

Ra_g^* : Modified Rayleigh number in gas phase ($= \dfrac{g\beta_g q_{conv} W_e^4}{\lambda_g \nu_g^2} Pr_g$) [-]

R_t : Turbulent Reynolds number $\left(= \dfrac{\kappa^2}{\nu\varepsilon} \right)$ [-]

R_y : Turbulent Reynolds number based on y $\left(=\frac{\sqrt{\kappa}y}{\nu}\right)$ [-]

T_c : Temperature at cooling plane [˚C, K]
T_g : Atmospheric temperature [˚C, K]
T_{rs} : Radiative temperature at gas-liquid interface [˚C, K]
T_s : Temperature at gas-liquid interface [˚C, K]
T_{sp} : Central temperature at gas-liquid interface [˚C, K]
T_w : Temperature at heating plane [˚C, K]
U_i : Velocity vector [m/s]
$\overline{u_i u_j}$: Reynolds stress [m²/s²]
$\overline{u_i t}$: Turbulent heat flux [m/sK]
V : Input voltage [V]
W_1 : Width of rectangular container [mm]
W_2 : Length of rectangular container [mm]
W_e : Characteristic length of rectangular container $\left(=4W_1W_2/2\left(W_1+W_2\right)\right)$ [mm]
X_i : Coordinates [m]

Greek Symbols

α : Thermal diffusivity of fluid [m²/s]
α_t : Turbulent thermal diffusivity of fluid [m²/s]
β : Volume expansion ratio of fluid [1/K]
δ : Fluid layer depth [mm]
δ_{ij} : Cronecker delta [-]
ε : Emissivity [-], Dissipation ratio [m²/s³]
λ : Thermal conductivity of fluid [W/mK]
ν : Kinetic viscosity of fluid [m²/s, cst]
ν_t : Turbulent viscosity of fluid [m²/s]
τ : time [s]

Subscription

cond : Based on thermal conduction
conv : Based on thermal convection
g : Gas
i : vector
j : vector
l : Liquid
rad : Based on thermal radiation
t : Turbulent

Superscription

- : Area-averaged, Time-averaged

3. Experimental Method and Numerical Computation

3.1 Experimental Apparatus and Measurement

The infrared equipment utilized in the present experiment is as follows: NEC SANEI TH3100MR; cooling system: Stirling engine, sensor type: Hg - Cd - Te, detection wavelength band: 8 - 13 [μm], effective temperature range: -50 ~ 2000 [˚C], image generation time: 0.75 [s], minimum detectable temperature: 0.1 [˚C]. In measurement, the time trace mode, which samples temperature data either over a horizontal scanning line or as points in a time series, was also utilized. A thermal image is composed of 239 horizontal scanning lines, and 3.125 [ms] is needed to measure and display each horizontal scanning line; the CRT display time of 1.25 [ms] is included in the scanning time of 3.125 [ms]. Therefore, it takes 3.125 [ms] × 239 lines (0.75 [s]) to acquire one thermal image. The infrared thermography system generates a two-dimensional thermograph representing radiative temperature, T_{rs}, as measured by the infrared sensor, on a color monitor. In general, the detection resolution for a pixel depends on the objective distance l, the distance between the object and the infrared sensor. For instance, when l = 1000 [mm], the horizontal resolution and the vertical resolution of the present infrared thermography are 1.13 [mm] and 1.32 [mm], respectively. Each scanning line has been calibrated to adjust the radiative temperature to the blackbody temperature based on a standard blackbody furnace.

Figure 1 shows a schematic of the experimental apparatus. To enable visualization of the thermal patterns formed at the gas-liquid interface, the heating part is composed of 10, 20 or 30 pieces of stainless foil (W_2 [mm] long × 10 [mm] wide × 30 [μm] thick) on bottom of a copper plate (1 [mm] thick), which was attached to the base of a rectangular container (open hydraulic area: W_1 [mm] long × W_2 [mm] wide, 20 [mm] thick) that was sufficiently insulated from the circumference except for at the free surface. The container was made of acrylic resin. Three different containers with aspect ratios of $W_1 \times W_2$ = 100 [mm] × 100 [mm] (Model I), 100 [mm] × 200 [mm] (Model II) and 100 [mm] × 300 [mm] (Model III) were prepared to evaluate the effect of aspect ratio on the heat transfer and fluid flow. The temperature at the heated plane was confirmed to be uniform when using the copper plate. As is shown in Fig. 2, the temperature was also measured using several pre-calibrated C-A thermocouples (100 [μm] in diameter) that were spot-welded at five points on the back of the copper plate. For all heating conditions, the temperatures of the thermocouples are almost the same as those used for the boundary conditions (standard deviation of about 0.25 [K]). Thus the temperature of the copper plate is basically heated uniformly. To estimate the heating loss from the bottom of the container, a heat flux sensor (VATELL BF – 04; size: 25 [mm] long × 25 [mm] wide, standard sensitivity: 10 [mV/(W/cm^2)], minimum detectable heat quantity: 0.008 [W/cm^2], effective temperature range: –50 ~ +180 [˚C]) was directly attached to the bottom. In this way, the net heat flux, q, to the gas-liquid interface could be adjusted. As the working fluid, the test equipment was filled with silicone oils of kinetic viscosities, v, of 30, 50, 100, 300 and 500 [cst] in order to investigate the effect on the heat transfer and fluid flow.

The fluid layer depth, δ, was also varied from 5, 10 and 15 [mm]. The maximum value of Joule heating was adjusted so that the temperature at the heated plane was about 80 [˚C] under each condition. The temperature at the gas-liquid interface was measured with infrared thermography, and the data was precisely modified by a calibration curve obtained between the true temperature and the radiative temperature. The temperature in the darkroom was measured with two C - A thermocouples (300 [μm] in diameter) installed between the infrared camera and the object. A series of experiments was carried out in the darkroom, where the infrared sensor was installed 0.45 [m] from the object. The measured object and the infrared sensor are installed in the enclosure simultaneously to attain the ideal measurement field by minimizing multiple reflections between the surrounding surfaces. The measurement field, in which the boundary walls were filled with an adiabatic material made of glass wool, was covered with pseudo-blackbody surfaces using textured black velvet. To maintain the temperature of the internal surfaces as much as possible, these were also covered with pseudo-blackbody surfaces to minimize multiple reflections. The atmospheric temperature therefore equals the surrounding wall temperature.

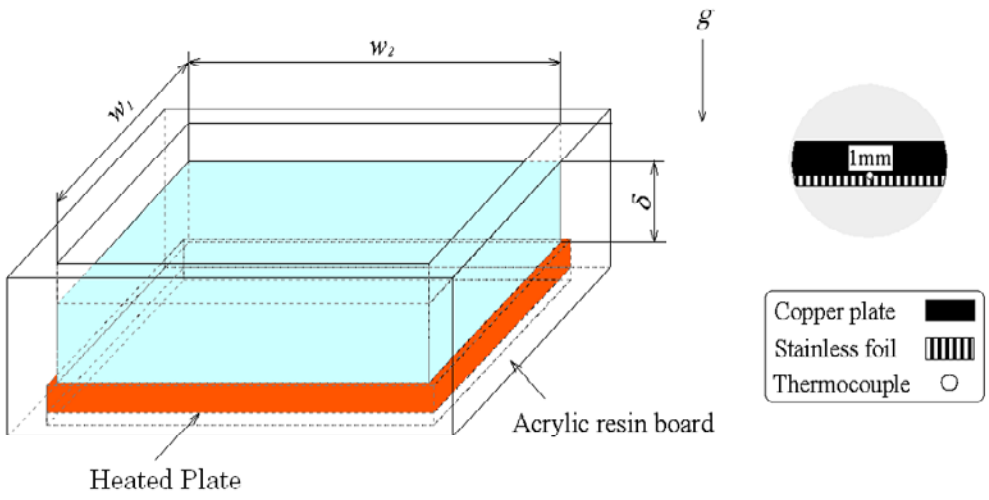

Fig. 1. Schematic of Experimental Apparatus.

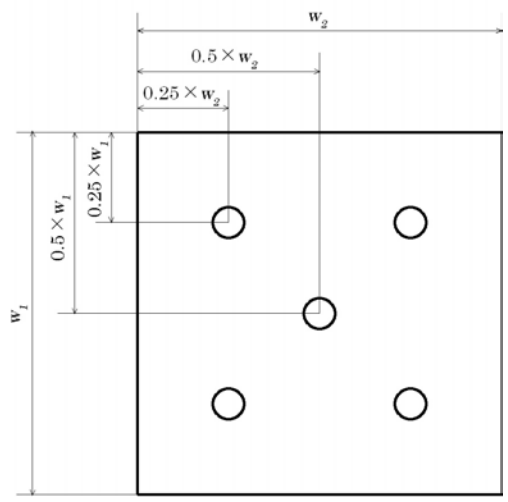

Fig. 2. Positioning of Thermocouples.

Figure 3 shows the energy balance at the gas-liquid interface. In general, we say that the energy balance at the gas-liquid interface is established as: q (net heat flux through the fluid layer) deduced from the loss to the bottom of the container = q_{rad} (radiative component) + q_{conv} (convective component). The fluid layer is under thermal conduction control until just before the appearance of Benard-cell: there is a linear temperature gradient between T_w and $\overline{T}_s$ in the fluid layer. The net heat flux at the gas-liquid interface under constant temperature of the heated plate can be described as:

$$q = \lambda_l \frac{\left(T_w - \overline{T}_s\right)}{\delta} \tag{1}$$

However, when the temperature field occurring at the gas-liquid interface becomes nonuniform after the appearance of Benard-cell or turbulent flow, the expression of the net heat flux can be converted to the following form of Joule heating:

$$q = \frac{VI}{A_0} - q_{loss} \tag{2}$$

where A_0, I and V are the area of the rectangular container (hydraulic area), the input current and the input voltage, respectively. q_{loss} is the loss to the bottom of the container as measured with the heat flux sensor. q_{rad} included in the expression of the energy balance at the gas-liquid interface is a radiative component and can be described as:

$$q_{rad} = \varepsilon\sigma\left(\overline{T}_s^{\,4} - T_g^{\,4}\right) \tag{3}$$

where the emissivity can be determined as follows (Inagaki et al., 2000):

$$a_s = \left(\frac{\overline{T}_{rs}}{\overline{T}_s}\right)^{4.3069} \tag{4}$$

$$\varepsilon = \frac{a_s - \left(T_g / \overline{T}_s\right)^{4.3069}}{1 - \left(T_g / \overline{T}_s\right)^{4.3069}} \tag{5}$$

where a_s, $\overline{T}_s$ and $\overline{T}_{rs}$ are the radiosity coefficient, the area-averaged temperature at the gas-liquid interface and the area-averaged temperature measured with the infrared device. The power index was determined by using a series of linear-approximated correlations between the energy detected by the infrared sensor and the temperature of a blackbody furnace. Since the approximated curve is displayed on a logarithmic scale, the power index that represents the inclination of the approximated curve is computed to 4 decimal places to provide sufficient accuracy (Inagaki, 2000). The value of the emissivity at the gas-liquid interface was determined as 0.98 from the above process. It is therefore considered that the present infrared thermography method is suitable for quantitative measurement of temperature and the convective heat transfer coefficient at the gas-liquid interface without the need for any special adjustment to the infrared device.

The area-averaged convective heat transfer coefficient or the area-averaged Nusselt number was obtained as follows at the gas-liquid interface:

$$h = \frac{q_{conv}}{\overline{T}_s - T_g} = \frac{q - q_{rad}}{\overline{T}_s - T_g} \tag{6}$$

$$Nu_g = \frac{hW_e}{\lambda_g} \tag{7}$$

Rayleigh number in the gas phase can also expressed as the following:

$$Ra_g^{\,*} = \frac{g\beta_g q_{conv} We^4}{\lambda_g \nu_g^{\,2}} Pr_g \tag{8}$$

in which the thermophysical properties included in the non-dimensional parameters were quantitatively estimated at a film temperature between $\overline{T}_s$ and T_g. Note that W_e has already been defined as the hydraulic diameter: $W_e = 4W_1W_2 / 2\left(W_1 + W_2\right)$.

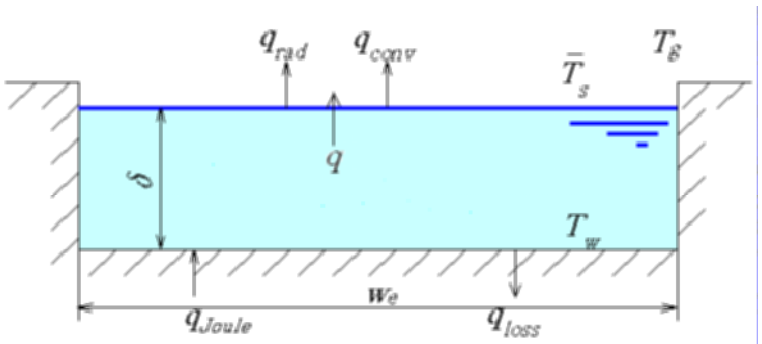

Fig. 3. Energy Balance at Gas-liquid Interface.

3.2 Measurement Uncertainty

Table 1 indicates the measurement uncertainty of the present data as relative values. The evaluation process is performed according to the ANSI/ASME Performance Test Codes (ASME, 1985).

Table 1. Measurement Uncertainty.

	W_e	T_w	T_s	T_g	q	q_{rad}	h	Nu_g	Nu_l	Ra_g^*	Ra_l
U_{ADD} (%)	1.0	1.8	3.0	1.8	4.5	4.4	7.0	7.2	6.9	5.4	5.0
U_{RSS} (%)	1.0	1.5	2.4	1.5	3.5	3.4	5.2	5.5	5.2	4.0	3.6
Degrees of freedom	> 30	> 30	> 30	> 30	> 30	> 30	> 30	> 30	> 30	> 30	> 30

3.3 Numerical Computation

Figure 4 shows the analysis model along with the coordinate system for the present numerical computation. As shown in Fig. 4 and Table 2, the boundary conditions are set to simulate the individual experimental situations as much as possible: the bottom (heated plate) is heated at a fixed temperature by Joule heating and the top (cooled surface) is cooled with a heat flux based on the energy balance at the gas-liquid interface. All four side-walls are insulated. For the initial conditions, the velocity over the entire analysis domain is zero and the fluid temperature equals the heated plate temperature. Since the cooled surface is a free interface, a slip boundary can be assumed. The k-ε model of low Reynolds number type (e.g., Lam-Bremhorst, 1981) is also applied to the present simulation to model turbulent flow conditions (see Table 3). The Boussinesq approximation is applied to the buoyancy term in the momentum equation, and the physical properties of the fluid are estimated at a film temperature between the heated plate temperature and the ambient temperature. A series of calculations is performed using the fully implicit method after transforming the governing transport equations of three-dimensional and steady state into difference equations by using the control volume method (Patankar, 1970). For the laminar flow calculation, the space mesh size is set at 2.0 [mm] (x and z directions) by 1.0 [mm] (y direction), and for the turbulent flow calculation, it is set at 1.0 [mm] (x and z directions) by 0.5 [mm] (y direction).

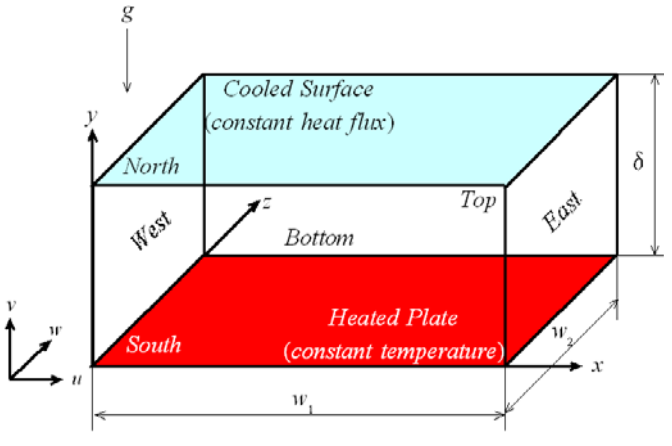

Fig. 4. Analysis Model along with Coordinate System.

Table 2. Boundary Conditions.

plane	Velocity	Temperature	Turbulent Kinetic Energy	Dissipation
North (Cooled plate)	$(\partial u, w/\partial y), v = 0$	$q = const(\le 0)$	$\frac{\partial k}{\partial y} = 0$	$\frac{\partial \varepsilon}{\partial y} = 0$
South (Heated plate)	$u, v, w = 0$	$T = T_w$	0	$\nu \frac{\partial^2 k}{\partial n^2}\Big\vert_w$
West & East (Adiabatic plate)	$u, v, w = 0$	$\frac{\partial T}{\partial n}\Big\vert_w = 0$	0	$\nu \frac{\partial^2 k}{\partial n^2}\Big\vert_w$
Top & Bottom (Adiabatic plate)	$u, v, w = 0$	$\frac{\partial T}{\partial n}\Big\vert_w = 0$	0	$\nu \frac{\partial^2 k}{\partial n^2}\Big\vert_w$

Table 3. Fundamental Equations for Two-Equation Turbulence Model Proposed by (Lam-Bremhorst, 1981).

$$\frac{D\overline{U}_i}{D\tau} = -\frac{1}{\rho}\frac{\partial \overline{P}}{\partial x_i} + \frac{\partial}{\partial x_j}\left(\nu \frac{\partial \overline{U_i}}{\partial x_j} - \overline{u_i u_j}\right) + g_i \beta\left(\overline{T} - \overline{T}_s\right)$$

$$-\overline{u_i u_j} = \nu_t\left(\frac{\partial \overline{U}_i}{\partial x_j} + \frac{\partial \overline{U}_j}{\partial x_i}\right) - \frac{2}{3}k\delta_{ij}$$

$$\nu_t = C_\mu f_\mu \frac{k^2}{\varepsilon}$$

$$\frac{D\overline{T}}{D\tau} = \frac{\partial}{\partial x_i}\left(\alpha \frac{\partial \overline{T}}{\partial x_i} - \overline{u_i t}\right)$$

$$\frac{Dk}{D\tau} = \frac{\partial}{\partial x_j}\left\{\left(\nu + \frac{\nu_t}{\sigma_k}\right)\frac{\partial k}{\partial x_j}\right\} + P_k - \varepsilon$$

$$\frac{D\varepsilon}{D\tau} = \frac{\partial}{\partial x_j}\left\{\left(\nu + \frac{\nu_t}{\sigma_\varepsilon}\right)\frac{\partial \varepsilon}{\partial x_j}\right\} + \frac{\varepsilon}{k}\left(C_{\varepsilon 1} f_1 P_k - C_{\varepsilon 2} f_2 \varepsilon\right)$$

$$P_k = -\overline{u_i u_j}\frac{\partial \overline{U}_i}{\partial x_j}$$

$$-\overline{u_i t} = \alpha_t \frac{\partial \overline{T}}{\partial x_i}$$

3.4 Precision of Numerical Computation

The heat transfer and fluid flow between two infinite horizontal plates (the bottom is uniformly heated and the top plane is uniformly cooled) are computed using the present numerical code to evaluate the quantitative applicability of infrared thermography (see Fig. 5). The computed results correlated with the conventional heat transfer correlations with a difference between them of 7% or less. The present numerical code is thus adequate in considering the characteristic phenomena treated in this paper.

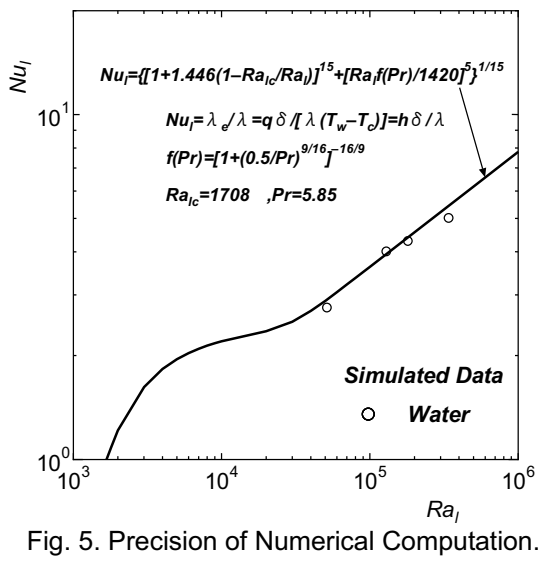

Fig. 5. Precision of Numerical Computation.

4. Results and Discussion

4.1 Visualization of Heat Transfer and Fluid Flow

Figures 6 ~ 8 show examples of the visualized thermal pattern at the gas-liquid interface when v = 100 [cst] and δ = 10 [mm] for Model I, Model II and Model III Several numerical and empirical conditions are shown in these figures. In general, a fluid is contained between two horizontal plates separated by a distance δ and uniformly heated according to T_{Lower} and T_{Upper}, respectively. As the temperature difference, ΔT (=T_{Lower} - T_{Upper}), determines heating of the fluid, the Rayleigh number, which represents heat transfer and fluid flow for natural convection in a horizontally enclosed space, is generally defined by the temperature difference and the distance. When the upper plate is maintained at a lower temperature than the lower plate, the heat source is the lower surface and the heat sink is the upper surface. However, according to the present boundary condition, the upper surface is a free interface which is in contact with the gaseous phase and is cooled by a uniform heat flux. In this research, the minimum temperature of the gaseous phase, i.e., the atmospheric temperature, T_g, is therefore adopted as the heat sink temperature. The Rayleigh number is defined by $\frac{g\beta_l(T_W - T_g)\delta^3}{\nu_l^2} Pr_l$ for the liquid phase. Table 4 indicates the critical Rayleigh number Ra_{lc} at which Benard-cell behavior begins to appear at the gas-liquid interface under each flow condition (The Japanese Society of Aerodynamics, 1997). The critical Rayleigh number is based on a temperature between the upper and lower sides, which are maintained at constant temperatures. For Model III at δ = 15 [mm], the present numerical computation implies that the cell pattern does not appear when Ra_l = 1037 (less than the critical value, 1124) but that it begins to appear when Ra_l = 1173 (more than the critical value, 1124). However, in the present case, since the upper side is cooled with a constant heat flux, these critical conditions are strictly inapplicable. Theoretically, the critical value for the object in this paper has not been clarified. The rate of the radiative heat flux from the gas-liquid interface to the feeding heat flux from the heated plate is estimated to be about 55% - 65% for all heating conditions and boundary conditions. In Figs. 6 ~ 8, the upper figure indicates the measured result and the lower the simulated result. These figures show that the number of cells decreases with an increase in the amount of Joule heating and that the simulated results are well correlated with the measured results. The consistency between the simulated results and the measured results is observed throughout all conditions: container aspect ratio, fluid viscosity and fluid layer depth.

Figure 9 shows an example of the empirically obtained transient temperature pattern at the gas-liquid interface when v = 100 [cst] and δ = 10 [mm] for Model I. These patterns were individually obtained at 0 [min], 28 [min], 51 [min] and 100 [min] for rapid heating of the heat transfer plate from 170 [W/m^2] to 589 [W/m^2]. The series of thermal patterns indicates a transient process in which the pattern of 16 cells initially begins to collapse, with coalescence occurring continuously until the pattern of 9 cells is formed.

Table 4. Critical Rayleigh Number, Ralc.

	Model I	Model II	Model III
δ [mm]	w_1:w_2 =1:1	w_1:w_2 =1:2	w_1:w_2 =1:3
5	1107	1104	1103
10	1124	1114	1111
15	1150	1129	1124

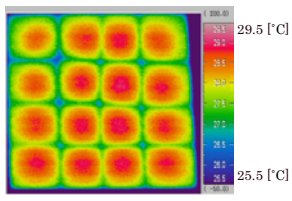

(a) $\overline{T}_s$ = 28.0 [°C]

q = 199.6 [W/m²]
Ra_l = 4.13 × 10³
Ra_g^* = 9.01 × 10⁶

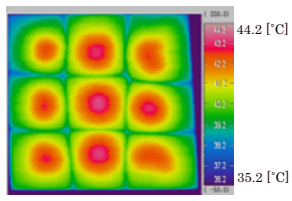

(b) $\overline{T}_s$ = 41.1 [°C]

q = 456.4 [W/m²]
Ra_l = 9.50 × 10³
Ra_g^* = 1.97 × 10⁷

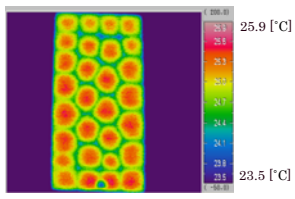

(c) $\overline{T}_s$ = 24.9 [°C]

q = 86.0 [W/m²]
Ra_l = 7.13 × 10³
Ra_g^* = 8.96 × 10⁶

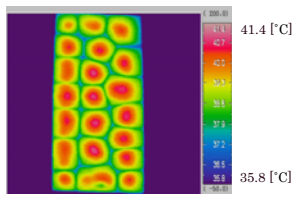

(d) $\overline{T}_s$ = 39.3 [°C]

q = 312.2 [W/m²]
Ra_l = 2.55 × 10⁴
Ra_g^* = 3.39 × 10⁷

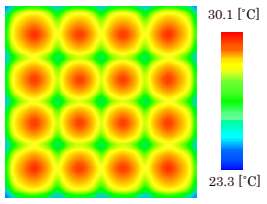

(a') $\overline{T}_s$ = 27.9 [°C]

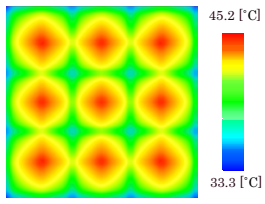

(b') $\overline{T}_s$ = 40.6 [°C]

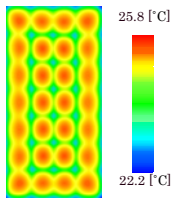

(c') $\overline{T}_s$ = 24.5 [°C]

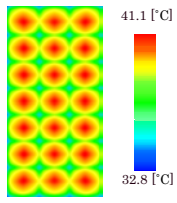

(d') $\overline{T}_s$ = 38.3 [°C]

((a) – (d): Measured Results, (a') – (d'): Simulated Results)

Fig. 6. Results for Experiment and Simulation (Model I ν = 100 [cst], δ = 10 [mm]).

Fig. 7. Results for Experiment and Simulation (Model II, ν = 100 [cst], δ = 10 [mm]).

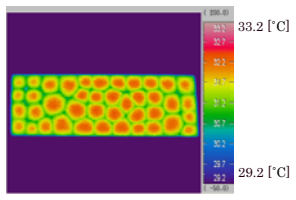

(e) $\overline{T}_s$ = 31.6 [°C]

q = 97.8 [W/m²]
Ra_l = 1.21 × 10⁴
Ra_g^* = 1.40 × 10⁷

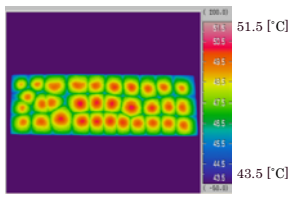

(f) $\overline{T}_s$ = 48.3 [°C]

q = 366.3 [W/m²]
Ra_l = 4.36 × 10⁴
Ra_g^* = 4.95 × 10⁷

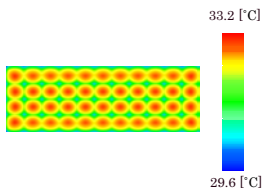

(e') $\overline{T}_s$ = 32.0 [°C]

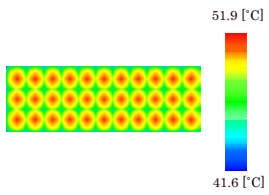

(f') $\overline{T}_s$ = 48.2 [°C]

Fig. 8. Results for Experiment and Simulation (Model III ν = 100 [cst], δ = 10 [mm]) ((e) – (f): Measured Results, (e') – (f'): Simulated Results).

Figure 10 shows an example of the empirically obtained transient temperature pattern at the gas-liquid interface when ν = 50 [cst] and δ = 15 [mm] for Model I. As is shown in Fig. 10(a), Benard-cell convection occurs continuously even if the amount of Joule heating is small. As shown in Figs. 10(b), (c) and (d), the flows become turbulent and the thermal patterns generated on the free surface become chaotic with an increase in the amount of Joule heating. In the visualization, the

amount of Joule heating was increased once every 1 [hour].

Figure 11 shows the fluctuating surface temperature at the center of the gas-liquid interface. The lower part of the figure corresponds to Fig. 10(a) and the upper to Fig. 10(d). Note that $\overline{T}_{sp}$ in the figure is the time-averaged temperature at the gas-liquid interface. The broken line indicates the measurement uncertainty for the present infrared sensing method. From this figure, it is confirmed that the fluctuations in temperature corresponding to the laminar condition of Fig. 10(a) are within the level of uncertainty. On the other hand, the temperature fluctuations corresponding to the turbulent condition of Fig. 10(d) are greater than the level of uncertainty. It can be seen that the thermal pattern formed at the gas-liquid interface has changed spatiotemporally: the flow condition has become turbulent.

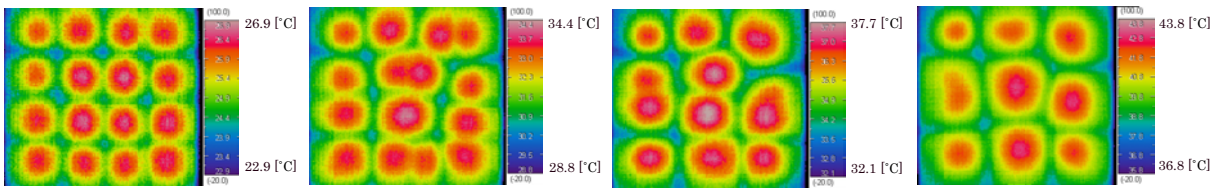

(a) 0 [min] after (b) 28 [min] after (c) 51 [min] after (d) 100 [min] after

Fig. 9. Empirically Obtained Transient Thermal Patterns
(Model I ν = 100 [cst], δ = 10 [mm], q = 170.0 [W/m2] → q = 589.0 [W/m^2]).

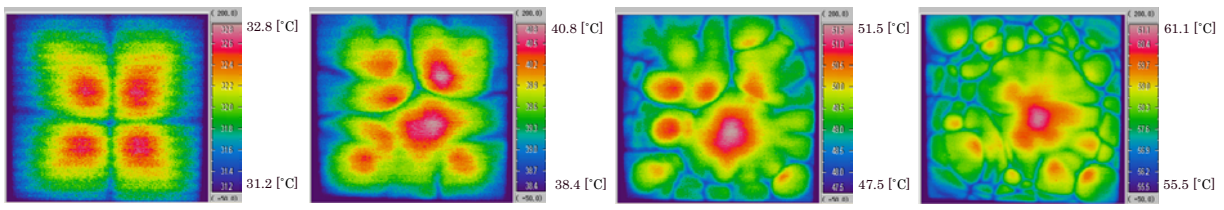

(a) Ra_l = 5.01 × 10^4
Ra_g^* = 4.25 × 10^7
q = 141.9 [W/m^2]
$\overline{T}_s$ = 31.9 [°C]

(b) Ra_l = 1.07 × 10^5
Ra_g^* = 4.76 × 10^7
q = 237.6 [W/m^2]
$\overline{T}_s$ = 39.6 [°C]

(c) Ra_l = 2.08 × 10^5
Ra_g^* = 8.74 × 10^7
q = 455.5 [W/m^2]
$\overline{T}_s$ = 49.7 [°C]

(d) Ra_l = 3.24 × 10^5
Ra_g^* = 1.26 × 10^8
q = 696.8 [W/m^2]
$\overline{T}_s$ = 58.8 [°C]

Fig. 10. Empirically Obtained Transient Thermal Patterns (Model I, ν = 50 [cst], δ = 15 [mm]).

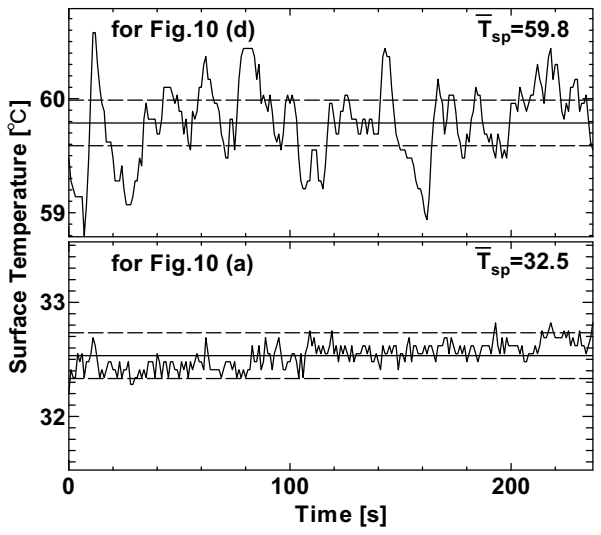

Fig. 11. Fluctuating Surface Temperature at the Center of the Gas-Liquid Interface.

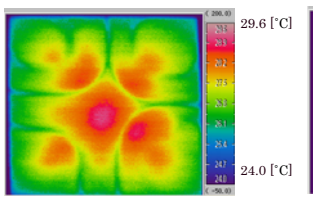

(a) $\overline{T}_s$ = 27.4 [°C]

v = 50 [cst]
q = 281.5 [W/m²]
Ra_l = 1.17 × 10⁵
Ra_g^* = 1.29 × 10⁷

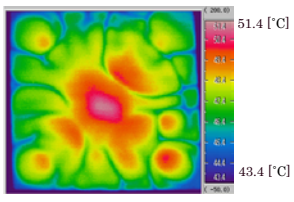

(b) $\overline{T}_s$ = 48.3 [°C]

v = 100 [cst]
q = 664.7 [W/m²]
Ra_l = 1.93 × 10⁵
Ra_g^* = 2.93 × 10⁷

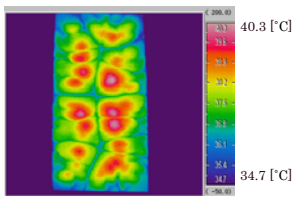

(a) $\overline{T}_s$ = 37.8 [°C]

v = 50 [cst]
q = 463.8 [W/m²]
Ra_l = 4.50 × 10⁵
Ra_g^* = 7.37 × 10⁷

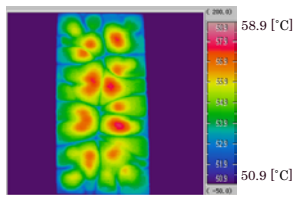

(b) $\overline{T}_s$ = 55.5 [°C]

v = 100 [cst]
q = 495.9 [W/m²]
Ra_l = 4.39 × 10⁵
Ra_g^* = 4.51 × 10⁷

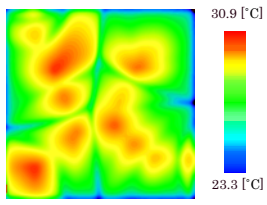

(a') $\overline{T}_s$ = 27.6 [°C]

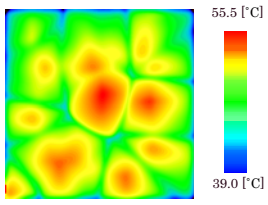

(b') $\overline{T}_s$ = 48.4 [°C]

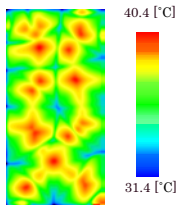

(a') $\overline{T}_s$ = 36.6 [°C]

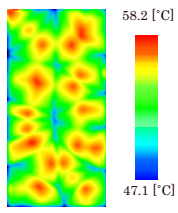

(b') $\overline{T}_s$ = 53.5 [°C]

((a) – (b): Measured Results, (a') – (b'): Simulated Results)

Fig. 12. Results for Experiment and Simulation (Model I, δ = 15 [mm]).

Fig. 13. Results for Experiment and Simulation (Model II, δ = 15 [mm]).

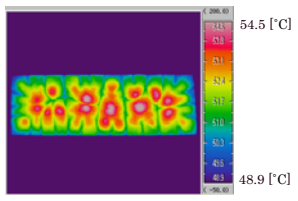

(a) $\overline{T}_s$ = 52.6 [°C]

v = 50 [cst]
q = 399.3 [W/m²]
Ra_l = 2.00 × 10⁵
Ra_g^* = 4.57 × 10⁷

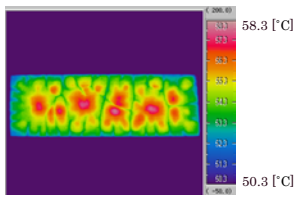

(b) $\overline{T}_s$ = 55.5 [°C]

v = 100 [cst]
q = 453.9 [W/m²]
Ra_l = 1.73 × 10⁵
Ra_g^* = 3.90 × 10⁷

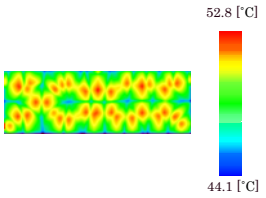

(a') $\overline{T}_s$ = 49.0 [°C]

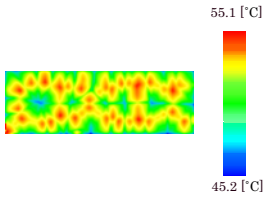

(b') $\overline{T}_s$ = 51.1 [°C]

Fig. 14. Results for Experiment and Simulation (Model III, δ = 15 [mm]) ((a) – (b): Measured Results, (a') – (b'): Simulated Results).

Figures 12, 13 and 14 show examples of the visualized thermal pattern at the gas-liquid interface for Model I, Model II and Model III respectively, when v = 50,100 [cst] and δ = 15 [mm] for the turbulent flow region. Again, the upper figure indicates the measured result and the lower the simulated result. These figures reveal that the thermal pattern empirically acquired by the

experimental investigation is similar to the pattern numerically determined by the computational investigation. Note that the influence of the difference in turbulence model on the simulated result seems a little small even when using other turbulence models (Chen, 1987, Wilcox, 1988, Yap, 1987).

Figures 15 (a), (b) indicate the influence of fluid viscosity on the visualized thermal pattern at the gas-liquid interface with the fluid layer depth and amount of heating fixed. These images were empirically obtained using the infrared thermography. There are no obvious differences between the two patterns, indicating that fluid viscosity does not affect heat transfer and fluid flow under the limited flow condition. Although the visualization was attempted several times under the same conditions, the same heat flow phenomenon appeared.

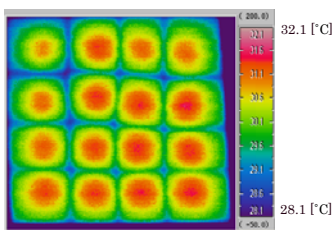

(a) v = 100 [cst]
$Ra_l = 5.16 \times 10^3$
$Ra_g^* = 1.21 \times 10^7$

$\overline{T}_s = 30.3$ [°C]

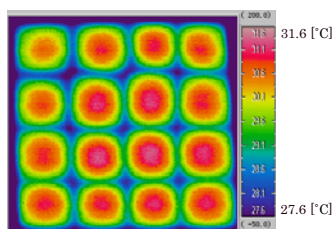

(b) v = 300 [cst]
$Ra_l = 5.37 \times 10^3$
$Ra_g^* = 1.29 \times 10^7$

$\overline{T}_s = 35.4$ [°C]

Fig. 15. Empirically Obtained Thermal Patterns (Model I, δ =10 [mm], q = 257.4 [W/m^2]).

Figures 16 (a) ~ (c) indicate the influence of fluid layer depth on the visualized thermal pattern at the gas-liquid interface with fluid viscosity and amount of heating of fixed. These images were empirically obtained using infrared thermography. Here, the number of cells decreases with increasing fluid layer depth and the fluid flow also becomes unstable. The deeper the fluid layer depth, the easier the transition to turbulent flow. This is for being easy to obtain an energy refilling from the fluid layer which became thick. Although the visualization was attempted several times under the same conditions, the same heat flow phenomenon appeared.

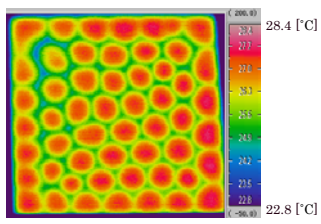

(a) δ = 5 [mm]
$Ra_l = 2.46 \times 10^3$
$Ra_g^* = 1.21 \times 10^7$

$\overline{T}_s = 26.3$ [°C]

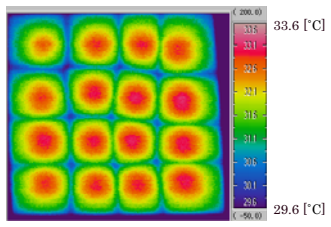

(b) δ = 10 [mm]
$Ra_l = 5.74 \times 10^3$
$Ra_g^* = 1.31 \times 10^7$

$\overline{T}_s = 31.8$ [°C]

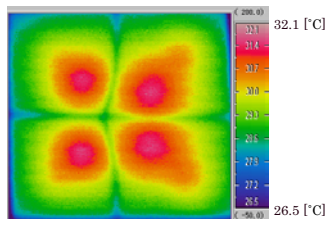

(c) δ = 15 [mm]
$Ra_l = 6.94 \times 10^4$
$Ra_g^* = 1.50 \times 10^7$

$\overline{T}_s = 29.9$ [°C]

Fig. 16. Empirically Obtained Thermal Patterns (Model I, ν = 100 [cst], q = 280.2 [W/m^2]).

4.2 Heat Transfer Measurement

Figure 17 shows the measured Nusselt number, Nu_g, discharged from the gas-liquid interface in terms of the modified Rayleigh number, $Ra_g{}^*$. These data include various container aspect ratios and hydraulic conditions in addition to the simulated result. Furthermore, several empirical heat transfer correlations previously proposed are illustrated as a reference:

(1) The heat transfer correlations describing the average Nusselt number of laminar natural convection along a vertical flat plate heated uniformly

Empirical correlation proposed by Vliet and Liu in 1969, $$Nu_g = \frac{5}{4}\left[0.60 Ra_g{}^{*0.2}\right] \quad (9)$$

Empirical correlation proposed by Goldstein and Eckert in 1960, $$Nu_g = \frac{5}{4}\left[0.513 Ra_g{}^{*0.2}\right] \quad (10)$$

(2) The heat transfer correlation describing the average Nusselt number of laminar natural convection along a horizontal flat plate heated uniformly

Empirical correlation proposed by Kitamura et al. in 1994,

$$1.6\times10^3 < Ra_g{}^* < 1.6\times10^7 \qquad Nu_g = 1.25 Ra_g{}^{*0.167} \quad (11)$$

$$1.6\times10^7 < Ra_g{}^* < 8.0\times10^8 \qquad Nu_g = 0.04 Ra_g{}^{*0.33} + 9.7 \quad (12)$$

It is obvious from Fig. 17 that there is not a large discrepancy between the above empirical correlations and the measured data and that the heat transfer coefficient is independent of container aspect ratio, fluid viscosity, amount of heating and fluid layer depth. That is, the coefficient of heat transfer can be summarized using a specific heat transfer correlation formula (using non-dimensional parameters) regardless of several conditions. A new heat transfer correlation for the gas-liquid interface is proposed as:

$$Nu_g = 0.38 Ra_g{}^{*0.24} \quad (13)$$

The present correlation also reveals that the heat transfer from the gas-liquid interface is independent of the characteristic length scale. Although the index 0.24 which accompanies the Rayleigh number is only the result of numerical fitting, it means that the local heat transfer coefficient expressed by Eq. (13) is little affected by characteristic length (equivalent diameter). This is because the characteristic length included in the non-dimensional numbers of Nu_g and $Ra_g{}^*$ almost cancels on each side of Eq. (13). Note that the coefficient of determination of the regression curve modeled by Eq. (13) is 0.6 for all of the measured data by using a statistical analysis.

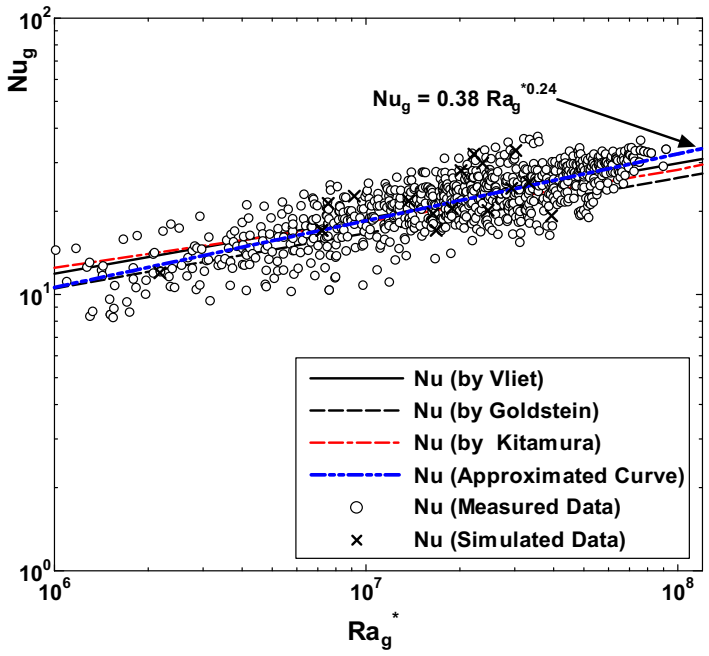

Fig. 17. Measured Average Nusselt Number.

5. Conclusion

Heat transfer and fluid flow Benard-cell convection in rectangular container with free surface was measured using infrared thermography. The nondestructive infrared thermography method was found to be effective in measuring and visualizing the temperature field generated at the gas-liquid interface. That is heat and fluid flow could be visualized at the gas-liquid interface. The visualized results correlate well with the results computed by simulation. Quantitative convective heat transfer measurement at the gas-liquid interface was also found to be possible using infrared thermography. A new heat transfer correlation is proposed for the gas-liquid interface of this system. The results imply that the coefficient of heat transfer can be summarized by a specific heat transfer correlation formula regardless of several conditions, including container aspect ratio, fluid viscosity and fluid layer depth.

References

American National Standard Institute and American Society of Mechanical Engineers 1985, Measurement Uncertainty, ANSI and ASME PTC19.1 (1985).

Asaeda, T., Tamai, N. and Takahashi, U., On the Thermal Convection of an Equilibrium State for Large Water Depth and Large Rayleigh Number, Japan Society of Civil Engineers, 323 (1982), 121-131.

Asaeda, T. and Tamai, N., On Characteristics of Plumes Observed in the Thermal Convection with the Large Rayleigh Number, Japan Society of Civil Engineers, 336 (1983), 65-73.

Cerisier, P., Rahal, S. and Rivier, N., Topological correlations in Benard-Marangoni convective structures, PHYSICAL REVIEW E, 54-5 (1996), 5086.

Chen, Y. S. and Kim, S. W., Computation of turbulent flows using an extended k-e turbulence closure model, NASA CR-179204 (1987).

Goldstein, R. J. and Eckert, E. R. G., Int. J. Heat Mass Transfer, 1 (1960), 208-218.

Inagaki, T. and Okamoto, Y., Measurement of Turbulent Heat Transfer Coefficients Using Infrared Thermography near Ambient Conditions and Its Quantitative Error Estimation, J. of JSME International, Series B, 42 (1999), 275.

Inagaki, T. and Ishii, T., On the Proposal of Quantitative Measurement by Using Three-colored Technique Combined with Several Infrared Sensors Having Different Detection Wavelength Bands, Int. J. of Infrared Physics & Technology, 41 (2000), 325.

Kamoi, A. and Okamoto, Y., Study on Variation of Thermal Image by Infrared Radiometer Influenced by Fluctuations of Environmental Factors, Journal of Visualization, 5-1 (2002), 95.

Kitamura, K. and Kimura, F., Proceedings of the Institution of Mechanical Engineers Part B, 60-570, (1994), 566.

Lam, C. K. G. and Bremhorst, K., A modified form of the k-ε model for predicting wall turbulence. J. Fluid. Engng., 103 (1981), 456.

The Japanese Society of Aerodynamics, The Aeromechanics Handbook (2nd Edition), (1997), 290.

Vliet, C. G. and Liu, C. K., An Experimental Study of Turbulent Natural Convection Boundary Layer, Trans. Am. Soc. Mech. Engrs. Series C, J. Heat Transfer, 91 (1969), 517.
Wilcox, D. C., Reassessment of the scale determining equation for advanced turbulence models, AIAA J., 26-11 (1988), 1299.
Yap, C., Turbulent heat and momentum transfer in recirculating and impinging flows, PhD Thesis, Faculty of Technology, University of Manchester, (1987).

Author Profile

Terumi Inagaki: He received B.E. (1984), and M.E. (1986) in Toyohashi University of Technology, D.E. (1991) in University of Tokyo. He is an associate professor (1996) in the department of mechanical engineering, Ibaraki University. His research interests are heat transfer, flow visualization, infrared sensing, non-destructive diagnosis and biological sensing.

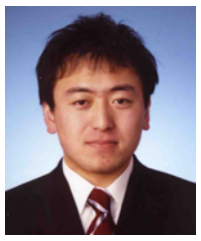

Masakazu Hatori: He received his B. E. in mechanical engineering in 2002 from Ibaraki University. He also received his M. E. in mechanical engineering in 2004 from Ibaraki University. He is now a member of Japan Nuclear Cycle Development Institute. His research interests are heat transfer, thermal visualization, Benard-cell convection, infrared sensing and measurement at gas-liquid interface.

Tomohiro Suzuki: He received his B. E. in mechanical engineering in 2004 from Ibaraki University. He will also receive his M. E. in mechanical engineering in 2006 from Ibaraki University. His research interests are heat transfer, thermal visualization, Benard-cell convection, infrared sensing and measurement at gas-liquid interface.

Yasuaki Shiina: He received the B.E. (1970), and M.E. (1973), D.E. (1990) in University of Tokyo. He is a senior scientist, department of advanced nuclear heat technology, Japan Atomic Energy Research Institute, and is also a guest professor of Tsukuba University.